



ELSEVIER

Combustion and Flame 135 (2003) 227–248

**Combustion  
and Flame**

# Micro-HCCI combustion: experimental characterization and development of a detailed chemical kinetic model with coupled piston motion

H. T. Aichlmayr<sup>1</sup>, D. B. Kittelson, M. R. Zachariah\*

*Departments of Mechanical Engineering and Chemistry and the Minnesota, Supercomputing Institute, The University of Minnesota, 111 Church St. SE, Minneapolis, MN 55455 USA*

Received 9 February 2003; received in revised form 15 June 2003; accepted 15 June 2003

## Abstract

Recent experimental and modeling work concerning Homogeneous Charge Compression Ignition (HCCI) combustion in small scales is presented. A zero-dimensional numerical model incorporating detailed chemical kinetics, heat transfer, blow-by, and a force balance is developed to interpret the experimental results and to explore HCCI combustion with a free-piston. The model consists of a new “Reactor Problem” for the sensitivity and kinetics component (Senkin) of the Chemkin software package. Following validation and interpretation of the experimental results, the model is used to conduct parametric studies. These studies and a non-dimensionalization of the governing equations yield parameters that characterize free-piston dynamics. These parameters are subsequently used to relate initial conditions to the percent mass lost. © 2003 The Combustion Institute. All rights reserved.

*Keywords:* Detailed chemical kinetic modeling; Homogeneous charge compression ignition combustion; Free piston; Auto-ignition

## 1. Introduction

Micro-engine-based power supplies can potentially deliver 10 W from 1 cm<sup>3</sup> packaged volumes [1] and replace batteries in various applications. Presently, four micro-engine programs are underway: The Micro-Gas Turbine Engine at the Massachusetts Institute of Technology [2]; The MEMS Rotary Engine at The University of California Berkeley [3]; The MEMS Free-Piston Knock Engine at Honeywell In-

ternational [1,4]; and the MEMS Free-Piston Engine-Generator at the Georgia Institute of Technology [5].

Small-scales present several challenges to the micro-engine designer. Quenching is perhaps the greatest concern because the specific heat transfer rate varies inversely with the characteristic dimension [6]. All micro-engine programs share this problem and their proposed solutions include: (1) fuels with wide flammability limits [7], (2) adiabatic boundaries [3], (3) multiple ignition points [5] and (4) Homogeneous Charge Compression Ignition (HCCI) combustion [1,4].

### 1.1. HCCI

HCCI is an engine combustion mode that entails compressing a fuel-air mixture until it explodes [8].

\* Corresponding author. Tel.: +1-612-626-9081; Fax: +1-612-625-6069.

*E-mail address:* mrz@me.umn.edu (M.R. Zachariah).

<sup>1</sup>Present address: Sandia National Laboratories, 7011 East Ave. Livermore, CA 94551.

**Nomenclature**

$A_B$	Bounce piston area (m <sup>2</sup> ), Eq. 1
$A_C$	Combustion piston area (m <sup>2</sup> ), Eq. 1
$A_c$	Cylinder cross-sectional area (m <sup>2</sup> ), Eq. 11
$A_p$	Piston cross-sectional area (m <sup>2</sup> ), Eq. 11
$A_s$	Surface area (m <sup>2</sup> ), Eq. 8
$A_t$	Gap area, $A_t = \frac{\pi}{4}(B^2 - D_p^2)$ (m <sup>2</sup> ), Eq. 4
$B$	Cylinder bore (mm)
$C_d$	Discharge coefficient (unitless), Eq. 4
$c$	Clearance distance, $c = \frac{V_c}{A_p}$ (mm)
$c_v$	Constant volume specific heat ( $\frac{\text{kJ}}{\text{kgK}}$ ), Eq. 7
$c_{v,k}$	Constant volume specific heat of species $k$ ( $\frac{\text{kJ}}{\text{kgK}}$ ), Eq. B.9
$D_p$	Piston diameter (mm)
$d$	Minimum distance between piston and end plug (mm), Eq. A.7
$F_x$	$x$ -Direction force (N), Eq. 1
$h$	Specific enthalpy ( $\frac{\text{kJ}}{\text{kg}}$ ), Eq. B.5
$I_L$	Leakage integral (unitless), Eq. 39
$k$	Species index (unitless), Eq. 7
$k_T$	Thermal conductivity ( $\frac{\text{W}}{\text{mK}}$ ), Eq. 10
$L$	Initial distance between piston and end plug (mm)
$M$	Compressible flow function, $M = M(P, P_\infty, \gamma)$ (unitless), Eq. 5
$M_L$	Percent mass lost (unitless)
$m_0$	Initial mass of cylinder contents, $m_0 = \frac{V_0}{u_0}$ (g), Eq. 32
$m_{cv}$	Mass of the control volume (kg), Eq. B.1
$m_f$	Final mass of cylinder contents (g), Eq. 32
$m_k$	Mass of species $k$ (kg), Eq. B.3
$m_p$	Piston mass (kg), Eq. 1
$\dot{m}$	Blow-by mass flow rate ( $\frac{\text{kg}}{\text{s}}$ ), Eq. 2
$\dot{m}_k$	Mass flow rate of species $k$ ( $\frac{\text{kg}}{\text{s}}$ )

$\dot{m}_k'''$	Mass volumetric rate of creation of species $k$ ( $\frac{\text{kg}}{\text{m}^3\text{s}}$ ), Eq. B.3
$N_s$	Total number of species (unitless), Eq. 7
$P$	Pressure (atm)
$P_0$	Initial pressure (atm), Eq. 17
$P_\infty$	Ambient pressure (atm)
$P_B$	Bounce chamber pressure (atm), Eq. 1
$P_C$	Combustion chamber pressure (atm), Eq. 1
$P^*$	Non-dimensional pressure, $P^* = \frac{P}{P_0}$ , Eq. 17
$\dot{Q}$	Heat transfer to the control volume (W), Eq. B.16
$\dot{q}$	Specific heat transfer rate ( $\frac{\text{W}}{\text{kg}}$ ), Eq. 7
$\bar{q}''$	Average heat flux ( $\frac{\text{W}}{\text{m}^2}$ ), Eq. 10
$R_m$	Mixture gas constant ( $\frac{\text{kJ}}{\text{kgK}}$ ), Eq. 4
$R_{\max}$	Ratio defined by $R_{\max} = \frac{r_{\text{cyl}}}{r_{\text{cyl}} - 1}$ (unitless), Eq. 24
$r$	Compression ratio, $r = \frac{V_t}{V_c}$ (unitless)
$r_{\text{cyl}}$	Maximum geometric compression ratio, $r_{\text{cyl}} = \frac{V_0}{V_c}$ (unitless), Eq. 24
$T$	Temperature (K)
$T_0$	Initial temperature (K), Eq. 17
$T_\infty$	Ambient temperature (K)
$T_w$	Uniform wall temperature (K), Eq. 10
$T^*$	Non-dimensional temperature, $T^* = \frac{T}{T_0}$ , Eq. 17
$t$	Time (s), Eq. 1
$t_0$	Reference time (s)
$t_G$	Piston-cylinder gap, $t_G = \frac{B - D_p}{2}$ (mm), Eq. 3
$t^*$	Non-dimensional process time, $t^* = \frac{t}{\tau_H}$ , Eq. 17
$t_c^*$	Non-dimensional cycle time, $t_c^* = \frac{\tau_C}{\tau_H}$ (unitless), Eq. 34

$U_{cv}$	Internal energy of the control volume (kJ), Eq. B.5
$U_d$	Minimum piston-end plug distance uncertainty (mm), Eq. A.8
$U_L$	Initial chamber distance uncertainty (mm), Eq. A.8
$U_r$	Compression ratio uncertainty (unitless), Eq. A.8
$U_{\bar{v}}$	Velocity uncertainty $\left(\frac{m}{s}\right)$ , Eq. A.4
$u$	Specific internal energy $\left(\frac{kJ}{kg}\right)$ , Eq. B.6
$u_k$	Specific internal energy of species $k$ $\left(\frac{kJ}{kg}\right)$ , Eq. 7
$V$	Volume ( $m^3$ )
$V_0$	Initial volume ( $m^3$ ), Eq. 18
$V_1$	Variable defined to obtain first-order ODEs $\left(\frac{m^3}{s}\right)$ , Eq. 15
$V_c$	Clearance volume ( $m^3$ )
$V^*$	Non-dimensional cylinder volume, $V^* = \frac{V}{V_0}$ , Eq. 17
$\tilde{V}$	Velocity $\left(\frac{m}{s}\right)$ , Eq. A.3
$v$	Specific volume $\left(\frac{m^3}{kg}\right)$
$v_0$	Initial specific volume $\left(\frac{kg}{m^3}\right)$ , Eq. 17
$v^*$	Non-dimensional specific volume, $v^* = \frac{v}{v_0}$ , Eq. 17
$\dot{W}$	Rate of work done on the control volume (W), Eq. B.15
$W_k$	Molecular weight of species $k$ $\left(\frac{g}{mol}\right)$ , Eq. 6
$x$	Cartesian coordinate (m), Eq. 1
$\dot{x}_0$	Initial piston velocity, $x_0 = \dot{x}(0)$ $\left(\frac{m}{s}\right)$
$Y_k$	Mass fraction of species $k$ (unitless)
$\Gamma$	Free-piston dynamic parameter, $\Gamma = \frac{LR_{max}A_p P_\infty}{m_p \dot{x}_0^2}$ (unitless), Eq. 28
$\Gamma_p$	Perfect gas dynamic parameter, $\Gamma_p = \frac{P_0 V_0}{(1-\gamma)m_p \dot{x}_0^2}$ (unitless), Eq. 30

$\gamma$	Specific heat ratio (unitless), Eq. 4
$\Delta t$	Time increment (s), Eq. A.2
$\Delta x$	Displacement (mm), Eq. A.1
$\delta t$	Camera temporal resolution (s), Eq. A.2
$\delta x$	Camera spatial resolution (mm), Eq. A.1
$\eta_{fc,i}$	Indicated fuel conversion efficiency (unitless)
$\tau$	Characteristic time (s), Eq. 17
$\tau_c$	Cycle time (s), Eq. 33
$\tau_H$	Half-cycle time, $\tau_H = \frac{LR_{max}}{\dot{x}_0}$ (s), Eq. 26
$\Phi$	Fuel-air equivalence ratio (unitless)
$\dot{\omega}_k$	Molar production rate of species $k$ $\left(\frac{mol}{cm^3 s}\right)$ , Eq. 6

HCCI has the following experimentally verified [9–11] features: (1) ignition occurs at several locations in the combustion chamber, (2) traditional flame propagation is absent, (3) the charge is consumed rapidly, (4) extremely lean mixtures can be ignited, and (5) fuel flexibility. Ignition depends upon the compression process and fuel oxidation kinetics [12]. Consequently controlling ignition timing is a challenge because it must be done indirectly. Additionally, HCCI suffers from poor power density and comparatively large CO and hydrocarbon emissions. Nonetheless, many efforts to adapt conventional engines to HCCI operation are underway because the possibility of simultaneously reducing  $NO_x$  emissions and increasing fuel economy exists [13]. In the context of micro-engines, however, HCCI is pursued because the charge can be ignited without a spark and consumed rapidly.

## 1.2. Free-piston engines

Employing a variable compression ratio is a promising approach to control HCCI ignition [14]. To implement this strategy, however, an unconventional engine configuration such as a free-piston is necessary [6,15–17]. A free-piston engine is depicted in Fig. 1A and one should note that the salient feature of this device is a mechanically unconstrained piston [18,19]. Hence the piston motion is determined exclusively by gas pressure forces (Fig. 1B). To illustrate, a force balance on the piston gives

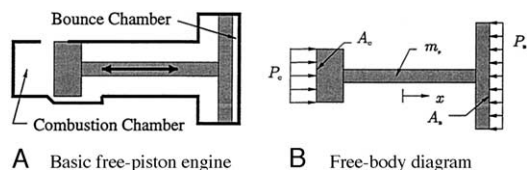


Fig. 1. The free-piston configuration. Note that a counterbalancing mechanism, work extraction scheme, and scavenging pump are omitted.

$$\sum F_x = m_p \frac{d^2x}{dt^2} = P_C A_C - P_B A_B, \quad (1)$$

where  $m_p$ ,  $P_C$  and  $P_B$  are the piston mass and the combustion- and bounce-chamber pressures, respectively.

## 2. Micro-HCCI experiments

To characterize HCCI combustion in small scales and to explore free-piston dynamics, single-shot experiments were conducted at Honeywell Laboratories in Plymouth, MN. The experiment is illustrated schematically in Fig. 2 and the principle is equally simple. A piston is driven into a cylinder filled with a combustible mixture and digital movies of the process are obtained. The movies capture visible emissions and provide temporal measurements of piston position and velocity.

### 2.1. Setup

Compressed air is used to accelerate a 5.238 g “hammer” in a stainless steel guide tube. The hammer collides with the injector pin and this in turn, impulses the piston. The cylinder is initially filled with a fuel-air mixture, consequently the piston compresses the charge until it explodes. Also, the design limits the injector pin travel to 2.54 mm.

A photograph of the piston and cylinder assembly is presented in Fig. 3. The piston is a machined steel gauge pin having a mass of 0.435 g. The piston is  $2.997 \pm 0.003$  mm in diameter and  $8.405 \pm 0.003$  mm long. The cylinders are Pyrex tubes that nominally have inside diameters of 3 mm. The actual dimensions of these tubes, however, vary consider-

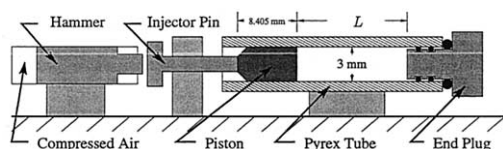


Fig. 2. Single-shot experiment schematic.

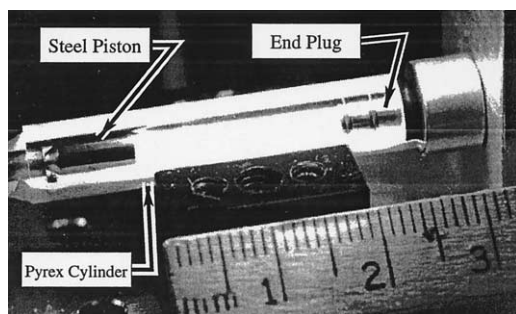


Fig. 3. Piston-cylinder assembly. The piston is on the left and the end plug is on the right.

ably. Consequently fit-tests are used to match cylinders to the piston. The optimal piston-cylinder combination occurs when the inside diameter of the cylinder and the outside diameter of the piston differ by approximately  $10 \mu\text{m}$ . Also, the piston is neither lubricated nor sealed, for example, with piston rings, but relies upon a gas layer separating piston and cylinder. This arrangement has mixed benefits: The piston motion is essentially frictionless (Fig. 1B), but at the expense of losing a significant amount of the fresh charge. The cylinder length (dimension  $L$  in Fig. 2) is typically between 25 and 57 mm and the cylinder is sealed by a brass plug and three O-rings.

Movies are obtained with a Vision Research Phantom v4.0 digital camera that is triggered by the actuation of a compressed air solenoid valve. The maximum sampling rate and temporal resolution of the camera are  $62,500 \text{ Pixels/s}$  and  $16 \mu\text{s}$ . The spatial resolution depends upon the camera position and it varies from 0.1 to 0.4 mm per pixel.

### 2.2. Qualitative results

Representative single-shot image sequences are presented in Figs. 4 and 5; several observations may be made. First, Fig. 4 conclusively demonstrates that combustion of a large alkane (heptane) in a space approximately 3 mm in diameter and 0.3 mm long is possible. This is noteworthy because the charge is initially at ambient conditions and the cylinder is neither insulated nor heated. Second, the piston is virtually stationary during combustion. Therefore, combustion is essentially a constant-volume process and one would expect the fuel conversion efficiency to approach the Otto cycle limit if the entire charge were consumed and heat transfer were negligible. Third, Fig. 5 demonstrates that micro-HCCI is capable of igniting mixtures that traditionally cannot be burned, that is, the equivalence ratio is 0.25. Fourth, although only part of the charge is consumed, Fig. 5

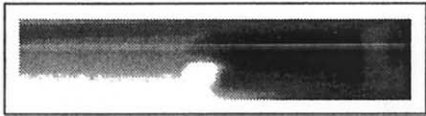
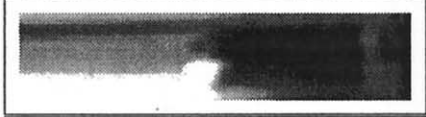
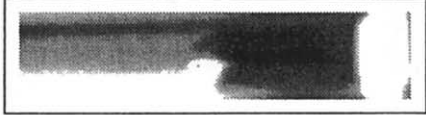
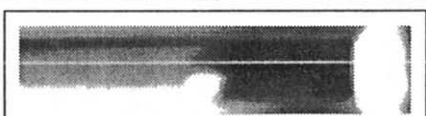
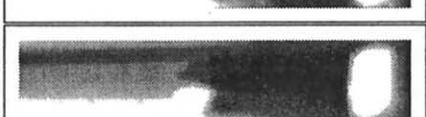
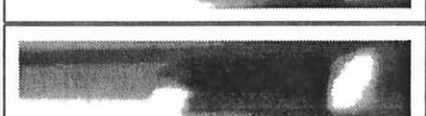
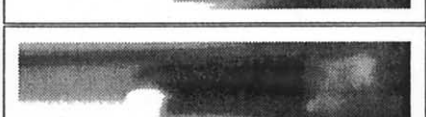
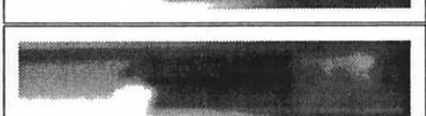
Image	Description
	Compression stroke, $t = t_0$ . Distance between piston and end plug: 1.1 mm.
	Compression stroke, $t = t_0 + 16 \mu\text{s}$ . Distance between piston and end plug: 0.5 mm.
	Ignition, $t = t_0 + 32 \mu\text{s}$ . Distance between piston and end plug: 0.3 mm.
	Combustion and beginning of the expansion stroke, $t = t_0 + 64 \mu\text{s}$ . Distance between piston and end plug: 0.5 mm.
	Expansion stroke, $t = t_0 + 96 \mu\text{s}$ . Distance between piston and end plug: 0.8 mm.
	Expansion stroke, $t = t_0 + 128 \mu\text{s}$ . Distance between piston and end plug: 1.1 mm.
	Expansion stroke, $t = t_0 + 160 \mu\text{s}$ . Distance between piston and end plug: 1.5 mm.
	Expansion stroke, $t = t_0 + 192 \mu\text{s}$ . Distance between piston and end plug: 1.9 mm.
	Expansion stroke, $t = t_0 + 224 \mu\text{s}$ . Distance between piston and end plug: 2.8 mm.
	Expansion stroke, $t = t_0 + 256 \mu\text{s}$ . Distance between piston and end plug: 3.3 mm.
	Expansion stroke and end of combustion, $t = t_0 + 288 \mu\text{s}$ . Distance between piston and end plug: 3.9 mm.

Fig. 4. A typical sequence of images from a single-shot experiment. The fuel is *n*-heptane and the equivalence ratio is 0.69. The charge was initially at room temperature and pressure. The dimension  $L$  is 57 mm. Refer to Fig. 2 for additional dimensions.

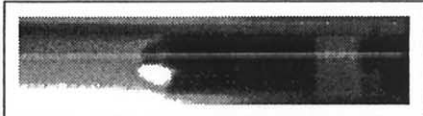
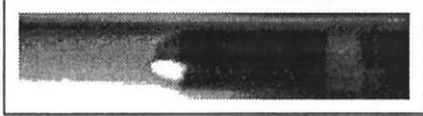
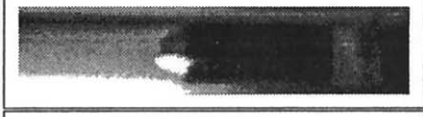
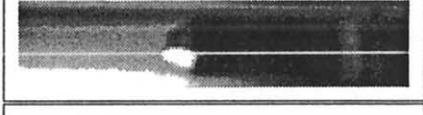
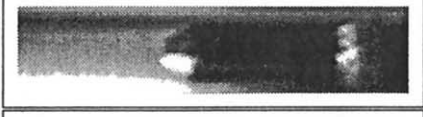
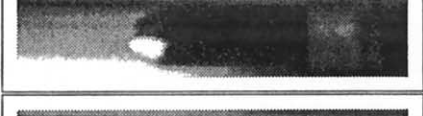
Image	Description
	Compression stroke, $t = t_0$ . Distance between piston and end plug: 1.7 mm.
	Compression stroke, $t = t_0 + 16 \mu\text{s}$ . Distance between piston and end plug: 1.5 mm.
	Compression stroke, $t = t_0 + 32 \mu\text{s}$ . Distance between piston and end plug: 0.9 mm.
	Compression stroke, $t = t_0 + 64 \mu\text{s}$ . Distance between piston and end plug: 0.8 mm.
	Compression stroke, $t = t_0 + 96 \mu\text{s}$ . Distance between piston and end plug: 0.4 mm.
	Combustion and beginning of the expansion stroke, $t = t_0 + 128 \mu\text{s}$ . Distance between piston and end plug: 0.7 mm.
	Expansion stroke, $t = t_0 + 160 \mu\text{s}$ . Distance between piston and end plug: 0.9 mm.
	Expansion stroke, $t = t_0 + 192 \mu\text{s}$ . Distance between piston and end plug: 1.2 mm.
	Expansion stroke, $t = t_0 + 224 \mu\text{s}$ . Distance between piston and end plug: 1.7 mm.
	Expansion stroke, $t = t_0 + 256 \mu\text{s}$ . Distance between piston and end plug: 2.2 mm.
	Expansion stroke and end of combustion, $t = t_0 + 288 \mu\text{s}$ . Distance between piston and end plug: 2.9 mm.

Fig. 5. A typical sequence of images from a single-shot experiment with a partial reaction. The fuel is *n*-heptane and the equivalence ratio is 0.25. The charge was initially at room temperature and pressure. The dimension  $L$  is 57 mm. Refer to Fig. 2 for additional dimensions.

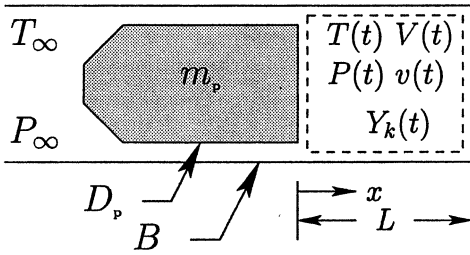


Fig. 6. Single-shot model diagram (dashed-line indicates the control surface).

suggests that ignition commences at the center of the combustion chamber and that HCCI proceeds through localized reactions.

**3. Development of a numerical model of the single-shot experiments**

In general, the single-shot experiment setup is too small for typical instruments, for example, pressure transducers, to be installed. Therefore a mathematical model must be relied upon to interpret the experimental results and to gain physical insight.

*3.1. Development*

The physical system under consideration is depicted in Fig. 6 and the following assumptions are made: (1) temperature, pressure, and species concentrations are uniform, (2) the gas escaping through the piston-cylinder gap (leakage or blow-by) may be described by one-dimensional quasi-steady compressible flow (Treating the gap flow like a Fanno flow problem is an alternate approach; this strategy is a necessity if the pressure drop in the piston-cylinder gap is appreciable.), (3) the compression process is quasi-static, (4) compressibility effects within the combustion chamber are negligible, and (5) conduction is the dominant heat transfer mode.

The model is developed by applying mass and energy balances to the gas and applying a force balance to the piston. The complete derivation is presented in Appendix B, but summarized here. First, a mass balance is applied to the control volume. The result is

$$\frac{1}{v} \frac{dV}{dt} - \frac{V}{v^2} \frac{dv}{dt} + \dot{m} = 0, \tag{2}$$

which relates the geometric volume,  $V$  and the specific volume,  $v$  to the mass flow rate of gas escaping through the piston-cylinder gap,  $\dot{m}$ . One should note that the gap dimension is defined by

$$t_G = \frac{B - D_p}{2}, \tag{3}$$

and that the gap area,  $A_t$  is given by Eq. B.2 in the Appendix. By assumption, the mass flow rate of escaping gas is given by

$$\dot{m} = \frac{C_d A_t P}{(R_m T)^{1/2}} M(P, P_\infty, \gamma), \tag{4}$$

where

$$M(P, P_\infty, \gamma) = \left\{ \left( \frac{P_\infty}{P} \right)^{\frac{1}{\gamma}} \left\{ \frac{2\gamma}{\gamma - 1} \left[ 1 - \left( \frac{P_\infty}{P} \right)^{\frac{\gamma-1}{\gamma}} \right] \right\}^{\frac{1}{2}} \right. \\ \left. \gamma^{\frac{1}{2}} \left( \frac{2}{\gamma + 1} \right)^{\frac{1}{2(\gamma-1)}} \right. \\ \left. \frac{P_\infty}{P} > \left( \frac{2}{\gamma + 1} \right)^{\frac{\gamma}{\gamma-1}} \right. \\ \left. \frac{P_\infty}{P} \leq \left( \frac{2}{\gamma + 1} \right)^{\frac{\gamma}{\gamma-1}} \right. \tag{5}$$

Next, species and energy balances are applied to the control volume and the blow-by is assumed to be homogeneous, that is,  $\dot{m}_k = \dot{m} Y_k$ . Consequently, the species balances are given by

$$\frac{dY_k}{dt} = v \dot{\omega}_k W_k, \tag{6}$$

where  $Y_k$ ,  $\dot{\omega}_k$ , and  $W_k$  are the mass fraction, molar production rate, and molecular weight of species  $k$ . Similarly, the energy balance is given by

$$c_v \frac{dT}{dt} + v \sum_{k=1}^N u_k \dot{\omega}_k W_k - \dot{q} + P \frac{dv}{dt} = 0, \tag{7}$$

where  $u_k$  is the internal energy of species  $k$ , and  $\dot{q}$  is the heat loss per unit mass.

The heat loss per unit mass is given by the product of the specific volume, average heat flux,  $\bar{q}''$  and the surface-area-to-volume ratio,  $A_s/V$  [6]. That is,

$$\dot{q} = v \bar{q}'' \left( \frac{A_s}{V} \right), \tag{8}$$

or

$$\dot{q} = \frac{v}{V} \left[ \frac{\pi B^2}{2} + \pi B(L - x) \right] \bar{q}'' \tag{9}$$

when expressed in geometric parameters.

The accuracy of the zero-dimensional heat loss model depends upon the method used to estimate the average heat flux. Although many techniques may be

employed, we assume that conduction is the dominant heat transfer mode. Consequently, we estimate the average heat flux by: (1) dividing a simplified representation for the combustion chamber, (2) solving the conduction equation to obtain a temperature field within the simplified domain, (3) computing initial heat fluxes at each boundary, (4) integrating these fluxes over their respective areas to obtain surface thermal energy transfers, (5) combining surface energy transfers and dividing the result by the total surface area to obtain an average heat flux.

Specifically, we assume that the fresh charge at any instant may be represented by an axisymmetric cylinder undergoing transient heating or cooling. Hence the cylinder is initially at the bulk temperature,  $T$  and the boundaries are held at the constant wall temperature,  $T_w$ . The conduction equation is subsequently solved using well-known analytical techniques and the result is a time-dependent double-infinite series [14]. However, only first term is retained when computing the initial heat fluxes at each boundary. These fluxes are next integrated over their respective surfaces, combined, and divided by the total surface area; this yields

$$\bar{q}'' = \frac{2k_T(T - T_w)}{(L - x)} \cdot \left[ \frac{0.440332\pi^2 + 5.09296 \left( \frac{L - x}{B} \right)^2}{\pi + 2\pi \left( \frac{L - x}{B} \right)} \right]. \quad (10)$$

One should note that although Eq. 10 is based upon *initial* heat fluxes, it is *quasi* time-dependent because  $x$  and  $T$  are functions of time. Also,  $k_T$  is the thermal conductivity of the fresh charge (assumed equal to air) and it varies with temperature.

Lastly, a force balance is applied to the piston. This yields

$$\frac{d^2V}{dt^2} = -\frac{A_c A_p (P_\infty - P)}{m_p}, \quad (11)$$

where  $m_p$ ,  $P_\infty$ ,  $A_c$  and  $A_p$  are the piston mass, the ambient pressure, and the cross-sectional areas of the cylinder and piston, respectively. The quantities  $A_c$  and  $A_p$  are defined by Eqs. B.20 and B.21 in the Appendix.

### 3.2. Implementation

To implement the single-shot model, Senkin [20] is modified to incorporate a new “reactor problem.” The problem consists of the differential equations

$$\frac{dT}{dt} = \frac{\dot{q}}{c_v} - \frac{P}{c_v} \frac{dv}{dt} - \frac{v}{c_v} \sum_{k=1}^{N_s} u_k \dot{\omega}_k W_k, \quad (12)$$

$$\frac{dY_k}{dt} = v \dot{\omega}_k W_k, \quad (13)$$

$$\frac{dV_1}{dt} = -\frac{A_c A_p (P_\infty - P)}{m_p}, \quad (14)$$

$$\frac{dV}{dt} = V_1, \quad (15)$$

$$\frac{dv}{dt} = \frac{v^2}{V} \dot{m} + \frac{v}{V} V_1, \quad (16)$$

along with the leakage and heat transfer models given by Eqs. 4, 9, and 10. In addition, Chemkin [21] subroutines provide the pressure and specific heat of the charge. For ease of use, the keyword input facilities and the post-processor are adapted to the new problem. Hence the user specifies  $T(0)$ ,  $P(0)$ , and  $Y_k(0)$  in the customary manner. The initial conditions  $v(0)$ ,  $V(0)$ , and  $V_1(0)$ , however, are derived from ancillary keyword inputs. One should note that  $V_1$  is introduced to make the system first order and that it is defined by Eq. 15. Also, a perfect gas (no combustion) model is obtained by deriving a system of equations comparable to Eqs. 12 through 16 and integrating them with Matlab.

### 3.3. Model validation and physical insights

The single-shot model is validated by simulating the experiment that yielded the image sequence presented in Fig. 4. The model parameters and their values are listed in Table 1. Although most of these quantities are direct measurements, one can argue that experimental uncertainties exaggerate discrepancies between model and experiment. In particular, the model is extremely sensitive to the initial velocity and the cylinder bore. Unfortunately, accurate determinations of the former quantity are difficult to obtain and measuring the latter quantity is altogether problematic.

#### 3.3.1. Validation

The piston position prediction is sensitive to the cylinder bore uncertainty. This is demonstrated in Fig. 7 by the perfect gas single-shot model. Hence discrepancies in the expansion path are probably a consequence of inaccurate cylinder bore estimates. This is plausible because the cylinder bore is *inferred* rather than *measured*. That is, to “measure” the cylinder bore, one inserts successively larger gauge pins into the cylinder until a “press fit” is achieved; the cylinder bore and gauge pin diameter are then as-

Table 1  
Parameter values employed to validate the single-shot model

Parameter	Value(s)	Unit	Origin	Status
Initial Velocity <sup>a</sup> ( $\dot{x}_0$ )	$41 \pm 8$	$\frac{\text{m}}{\text{s}}$	Measurement	Fixed
Chamber Length ( $L$ )	$57.00 \pm 0.03$	$\frac{\text{s}}{\text{mm}}$	Measurement	Fixed
Equivalence ratio ( $\Phi$ )	0.69	NA	Assumption	Fixed
Fuel (Kinetic Mechanism)	Heptane [22]	NA	Assumption	Fixed
Discharge Coefficient <sup>b</sup> ( $C_d$ )	0 and 1	NA	Assumption	Fixed
Initial Temperature ( $T_0$ )	300	K	Assumption	Fixed
Initial Pressure ( $P_0$ )	1	atm	Assumption	Fixed
Piston Mass ( $m_p$ )	$0.431 \pm 0.001$	g	Measurement	Fixed
Clearance Volume <sup>c</sup> ( $V_c$ )	$0.71591\text{E-}03$	$\text{cm}^3$	Estimate	Fixed
Piston Diameter ( $D_p$ )	$2.997 \pm 0.003$	mm	Measurement	Fixed
Cylinder Bore <sup>d</sup> ( $B$ )	$3.007 \pm 0.003$	mm	Measurement	Adjusted
Wall Temperature ( $T_w$ )	300	K	Assumption	Fixed

<sup>a</sup> Mean values, for example,  $41 \frac{\text{m}}{\text{s}}$ , are used by the model.

<sup>b</sup> This parameter is set to 0.0 and 1.0 to obtain the “No Leakage” and “Leakage” and solutions, respectively.

<sup>c</sup> The clearance volume is assumed equal to the annular region between the end plug and cylinder.

<sup>d</sup> Using gauge pins, this dimension was estimated to be  $3.004 \pm 0.003$  mm. This estimate, however, was increased by 0.003 mm to improve model-experiment correspondence.

sumed equal. Consequently, this measurement is somewhat subjective and longitudinal variations in the cylinder bore are impossible to detect. Therefore we adjust the cylinder bore by the experimental uncertainty, that is, from 3.004 to 3.007 mm, to maximize model-experiment correspondence during the expansion stroke.

Although this is not done, one could also justify adjusting the piston initial velocity. These measurements are relatively inaccurate (Appendix A) and the model is unfortunately very sensitive to them. This is demonstrated in Fig. 8 with the perfect gas model.

Hence a slightly inaccurate initial velocity could markedly skew the model prediction. Fortunately, the actual measurement, that is,  $41 \frac{\text{m}}{\text{s}}$ , yields excellent model-experiment correspondence.

Predicted and experimental results are compared in Figs. 9–11. These plots demonstrate that model and experiment correspond well. One should note that increasing the cylinder bore by 0.003 mm is the only adjustment made. Moreover, position and velocity predictions are well within the bounds of experimental uncertainty (Appendix A).

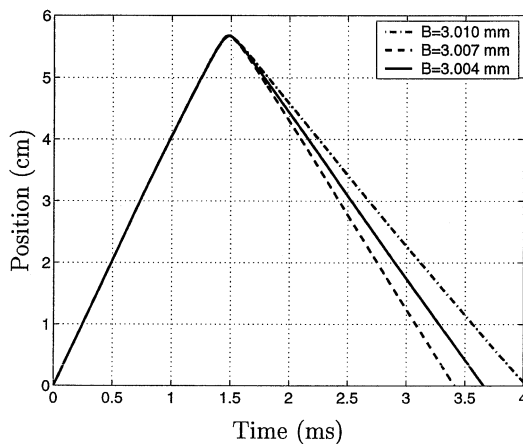


Fig. 7. Sensitivity of the piston position prediction to the cylinder bore uncertainty ( $\gamma = 1.3175$  in the perfect gas model).

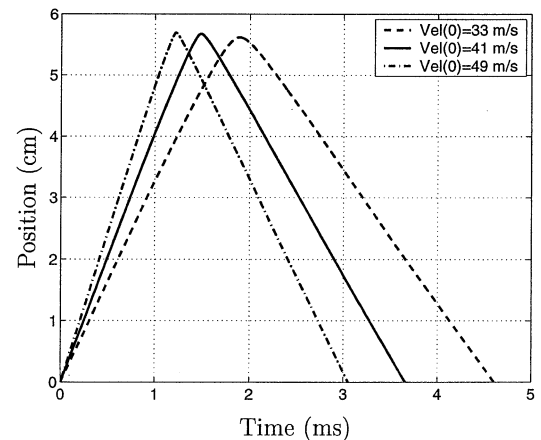


Fig. 8. Sensitivity of the piston position prediction to the initial velocity uncertainty ( $\gamma = 1.3175$  in the perfect gas model).

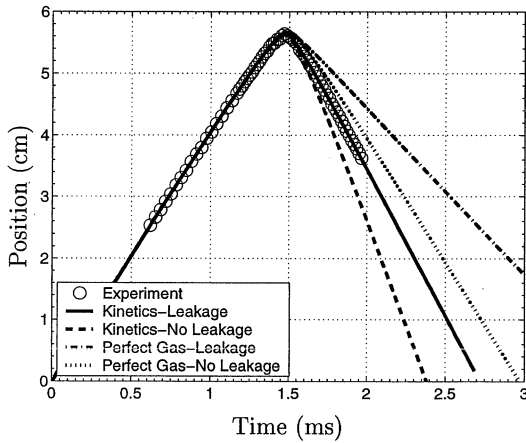


Fig. 9. A comparison of piston position data obtained from the images shown in Fig. 4 and single-shot model predictions. Assumed model parameters are listed in Table 1. Error bars are omitted for clarity, but uncertainties in position and time are 0.1 mm and 16  $\mu$ s. The perfect gas model assumes  $\gamma = 1.3175$ .

3.3.2. Physical insights

The numerical model provides many physical insights into the single-shot experiments. To demonstrate, the following cases are considered: (1) detailed kinetics with leakage, (2) detailed kinetics without leakage, (3) perfect gas with leakage, and (4) perfect gas without leakage. These cases are plotted in Figs. 9–11 with the experimental results.

First, all cases in Figs. 9 and 10 give similar

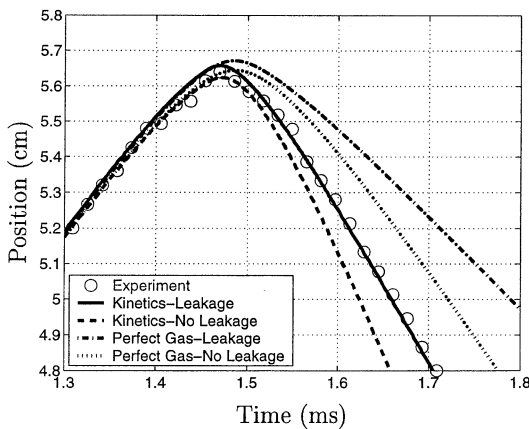


Fig. 10. A comparison of piston position data obtained from the images shown in Fig. 4 and single-shot model predictions in detail. Assumed model parameters are listed in Table 1. Error bars are omitted for clarity, but uncertainties in position and time are 0.1 mm and 16  $\mu$ s. The perfect gas model assumes  $\gamma = 1.3175$ .

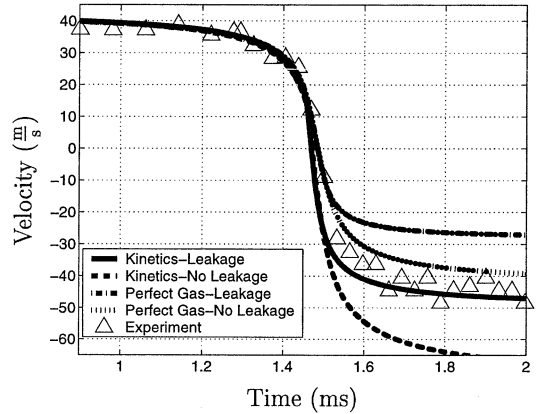


Fig. 11. A comparison of piston velocity data obtained from the images shown in Fig. 4 and single-shot model predictions. Assumed model parameters are listed in Table 1. Error bars are omitted for clarity, but uncertainties in time and velocity are 16  $\mu$ s and 20–50%, respectively. The largest uncertainties are obtained when the piston reverses direction (1.4–1.6 ms). The perfect gas model assumes  $\gamma = 1.3175$ .

predictions for the compression path, but the expansion paths vary greatly. This occurs because most of the mass loss because of blow-by occurs when the piston reverses direction. To demonstrate, percent mass lost predictions by the kinetics and perfect gas models are plotted in Fig. 12. These curves suggest that approximately 40% of the charge is lost when the piston reverses direction (circa 1.5 ms). Hence the charge mass essentially undergoes a step change at maximum compression ratio. Therefore, position traces will be identical during the compression stroke, but differ in the expansion stroke.

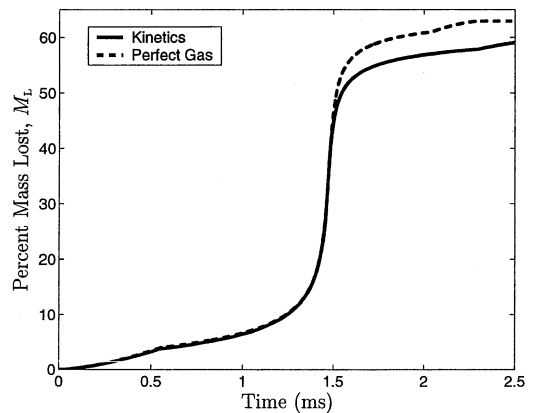


Fig. 12. Percent mass lost prediction corresponding to the images presented in Fig. 4. Model parameters are listed in Table 1.

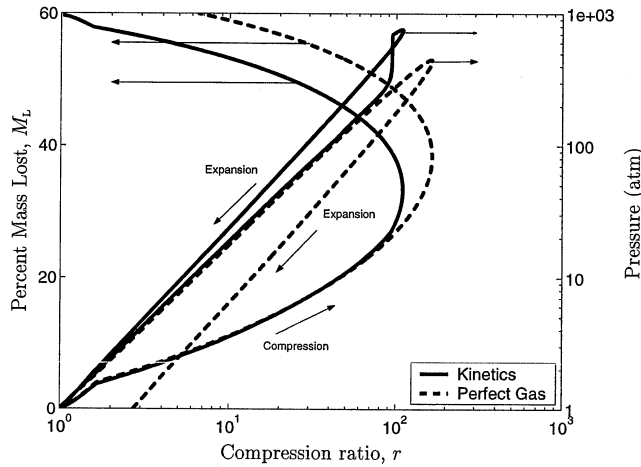


Fig. 13. Pressure and percent mass lost predictions corresponding to the images presented in Fig. 4. Model parameters are listed in Table 1.

Comparing kinetics and perfect gas curves in Fig. 12 yields another interesting insight: Combustion apparently *decreases* the percent mass loss. Intuitively, one would expect the opposite to be true because combustion increases the temperature and pressure; therefore the pressure gradient and the blow-by mass flow rate should increase. This result can be clarified, however, by plotting the percent mass lost and pressure versus compression ratio in Fig. 13.

The key to understanding this counterintuitive result is to recognize that the compression ratio *varies*. To illustrate, the curves representing the kinetics and perfect gas results in Fig. 13 coincide until the compression ratio is approximately 90:1 that is, the percent mass lost predictions are identical. But when a volumetric compression ratio of 90:1 is attained, the kinetics model predicts that the charge explodes and that the pressure rises above the perfect gas case. When a free-piston is employed, this additional pressure rise causes the piston to decelerate faster than the perfect gas case. Hence the piston is brought to rest at a compression ratio of approximately 100:1. This greater deceleration also implies that the piston spends less time at maximum compression ratio (see Fig. 10). Therefore, when combustion occurs, the piston spends less time at large compression ratios and pressures, which in turn yields less mass loss than the perfect gas case. Alternatively, if the compression ratio were fixed for example, in a crank engine, then the residence times would be identical and combustion would maximize the mass lost.

Second, a comparison of “Leakage” and “No-Leakage” curves in Fig. 10 reveals that the volumetric compression ratio *increases* when mass is lost. This phenomena is a consequence of mass loss alter-

ing the relationship between density and volume (Eq. 2). That is, in both cases the charge is compressed to the same density, but the charge occupies a smaller volume when mass is lost.

Third, the predicted temperature history is plotted in Fig. 14. Ignition is indicated by a sudden temperature rise and one should note that timing is mildly affected by mass loss. This is an expected result because most mass loss occurs after ignition (Fig. 12). On the other hand, mass loss causes product temperatures to decrease faster during the expansion stroke.

Finally, the predicted pressure-volume (P-V) diagram is plotted in Fig. 15. This diagram suggests that the single-shot process is a fair approximation to an Otto cycle when the entire charge is retained. Alternatively, Fig. 15 demonstrates that mass loss signif-

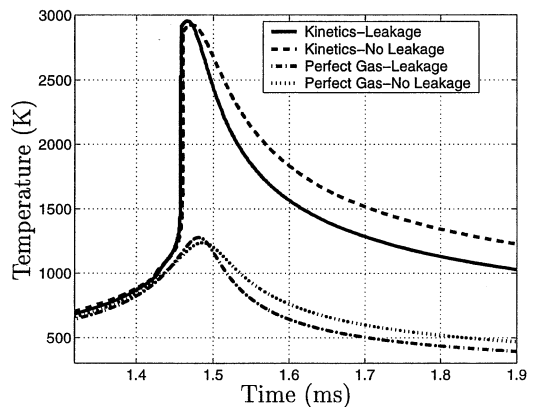


Fig. 14. Predicted charge temperatures for conditions corresponding to Fig. 4. Model parameters are listed in Table 1.

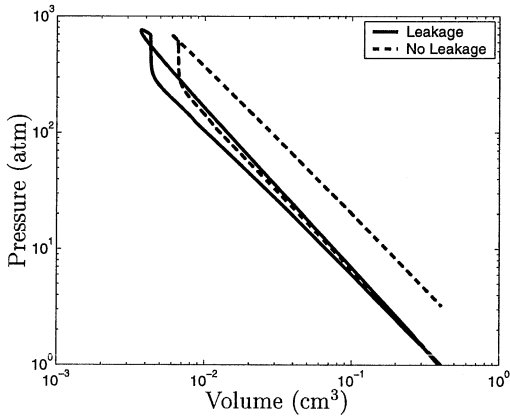


Fig. 15. Predicted P-V diagram for conditions corresponding to Fig. 4. Model parameters are listed in Table 1.

icantly decreases the cycle work. Therefore, mass loss is a serious concern for any micro-engine design that employs gas compression. Consequently devising an effective seal or mitigating the problem is an essential step toward developing a micro-engine.

Quenching is an equally significant concern for micro-engine development. Our heat loss model (Eqs. 9 and 10) is based upon conduction heat transfer. Consequently it maximizes the heat flux from the charge to the walls and it represents a “worst case” scenario in terms of *bulk heat loss* [14]. Although our model depends upon the surface-area-to-volume ratio, it does not capture the localized quenching of chemical reactions for example, in boundary regions. To do this, one would need to evaluate a multi-dimensional energy equation, estimate the flow field, and possibly consider species transport. Such a formulation, however, would greatly increase the complexity of the single-shot model and may not yield a

clear benefit. That is, the success of our model suggests that quenching may not be a significant factor in the length- and time-scales considered.

#### 4. Single-shot parametric model study

To gain further insight, a parametric study is conducted to find relationships between initial conditions and overall results; the details are summarized in Table 2. The percent mass lost ( $M_L$ ) and the indicated fuel conversion efficiency ( $\eta_{fc,i}$ ) are of particular interest and the results are plotted in Figs. 16 and 17.

Efficiency and percent mass lost have complimentary features. For example, Fig. 16 demonstrates that the percent mass lost decreases with chamber length ( $L$ ) and Fig. 17 demonstrates that maximum efficiencies are obtained with the longest chamber length (9.0 cm). Therefore, maximum efficiency corresponds to minimum mass lost. Also, Fig. 16 suggests that mass loss is relatively insensitive to the fuel and Fig. 17 indicates that this is also true for efficiency. In contrast, the percent mass lost is relatively insensitive to the equivalence ratio (Fig. 16) while the indicated fuel conversion efficiency is not (Fig. 17).

Mass loss has a greater influence on efficiency than the compression ratio. For instance, one expects efficiencies to increase with compression ratio, but in Fig. 17, efficiencies are maximized when the compression ratio is smaller than 200. To clarify this phenomena, indicated efficiencies for cases with  $\Phi = 0.95$  are plotted in Figs. 18 and 19. A comparison of these plots reveals that mass loss causes the efficiency to peak when  $50 \leq r \leq 100$ . Also, cases without mass loss (Fig. 19) confirm that the combination of HCCI combustion and a free-piston approximates an ideal Otto cycle for compression ratios

Table 2  
Parametric study model inputs

Parameter	Value(s)	Unit
Initial velocity ( $\dot{x}_0$ )	5, 10, 15, 20, 25, 30, 35, 40, 45, 50	$\frac{m}{s}$
Chamber length ( $L$ )	0.6, 1.5, 3.0, 4.5, 7.5, 9.0	$\frac{cm}{cm}$
Equivalence ratio ( $\Phi$ )	0.25, 0.47, 0.69, 0.95, 1.5, 2.9	NA
Fuel (kinetic mechanism)	Heptane and Propane [23]	NA
Discharge coefficient ( $C_d$ )	0 and 1	NA
Initial temperature ( $T_0$ )	300	K
Initial pressure ( $P_0$ )	1	atm
Piston mass ( $m_p$ )	0.431	g
Clearance volume ( $V_c$ )	0.71591E-03	$cm^3$
Piston diameter ( $D_p$ )	0.29972	cm
Cylinder bore ( $B$ )	0.300228	cm
Wall temperature ( $T_w$ )	300	K

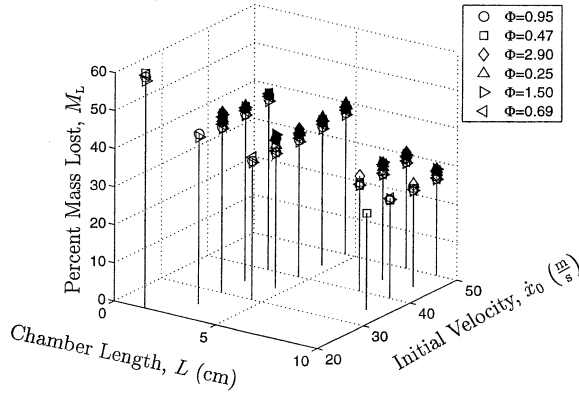


Fig. 16. Predicted percent mass lost versus chamber length and initial velocity for cases in which the charge ignites; open symbols indicate heptane-air and dark symbols indicate propane-air.

smaller than 100:1, which incidentally, is consistent with trends observed in conventional engines.

### 5. Non-dimensional analysis

To reduce the size of the parameter space and to uncover natural interdependencies, we non-dimensionalize the model equations. First, the non dimensional variables are defined. Let

$$V^* = \frac{V}{V_0}, t^* = \frac{t}{\tau}, v^* = \frac{v}{v_0}, T^* = \frac{T}{T_0}, \text{ and } P^* = \frac{P}{P_0}, \tag{17}$$

where  $V_0, v_0, T_0$  and  $P_0$  represent initial values (The initial volume is given by

$$V_0 = A_P L + V_C. \tag{18}$$

Hence the volume of the piston-cylinder gap is neglected.) and  $\tau$  is a characteristic time. Next, if one assumes that  $P_0 = P_\infty$  and  $T_0 = T_\infty$ , then the non-dimensional forms of Eqs. 2, 6, 7, B.22, and B.23 are given by

$$\frac{dY_k}{dt^*} = v^* v_0 \tau \dot{\omega}_k W_k, \tag{19}$$

$$\begin{aligned} \frac{dT^*}{dt^*} + \frac{v_0 T}{c_v T_0} v^* \sum_{k=1}^{N_s} u_k \dot{\omega}_k W_k - \frac{\dot{q} \tau}{c_v T_0} + \frac{P_0 v_0}{c_v T_0} P^* \frac{dv^*}{dt^*} \\ = 0, \end{aligned} \tag{20}$$

$$\frac{dv^*}{dt^*} = \frac{\tau v_0 \dot{m}}{V_0} \frac{v^{*2}}{V^*} + \frac{v^*}{V^*} \frac{dV^*}{dt^*}, \tag{21}$$

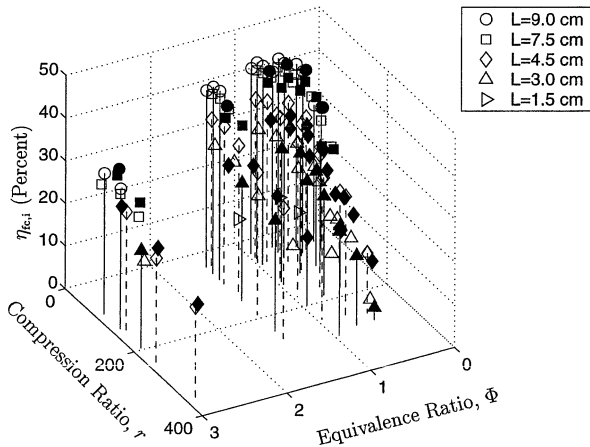


Fig. 17. Predicted indicated fuel conversion efficiency versus compression ratio and equivalence ratio when the model includes blow-by. Open symbols indicate heptane-air and dark symbols indicate propane-air mixtures.

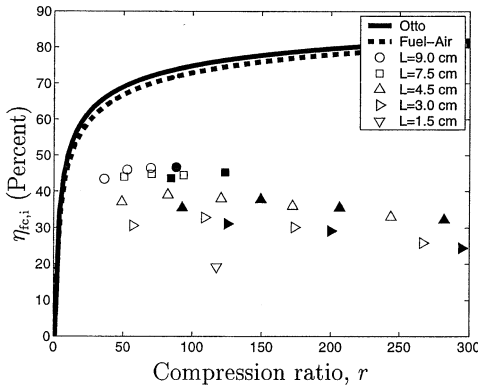


Fig. 18. Predicted indicated fuel conversion efficiency versus compression ratio with mass loss and  $\Phi = 0.95$ . Open symbols indicate heptane-air and dark symbols indicate propane-air. The Otto cycle efficiency is computed by assuming  $\gamma = 1.3$ . Heptane is used in the fuel-air cycle computations.

$$\frac{dV^*}{dt^*} = -\frac{\dot{x}\tau}{LR_{\max}}, \quad (22)$$

and

$$\frac{d^2V^*}{dt^{*2}} = \frac{\tau^2 P_\infty}{LR_{\max} \left(\frac{m_p}{A_p}\right)} (P^* - 1), \quad (23)$$

respectively. One should note that  $R_{\max}$  is defined by

$$R_{\max} = \frac{r_{\text{cyl}}}{r_{\text{cyl}} - 1}, \quad (24)$$

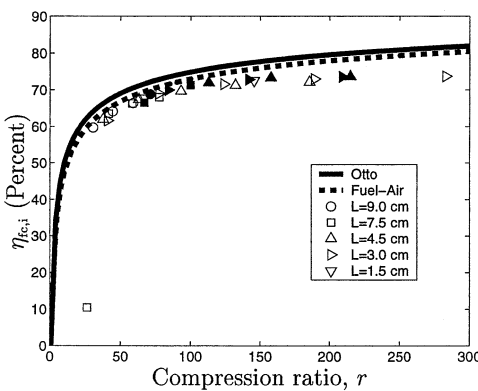


Fig. 19. Predicted indicated fuel conversion efficiency versus compression ratio without mass loss and  $\Phi = 0.95$ . Open symbols indicate heptane-air and dark symbols indicate propane-air. The Otto cycle efficiency is computed by assuming  $\gamma = 1.3$ . Heptane is used in the fuel-air cycle computations.

where  $r_{\text{cyl}} = V_0/V_c$  and  $V_c$  is the clearance volume. Thus,  $r_{\text{cyl}}$  is the maximum compression ratio that can be achieved with a given piston and cylinder. (One should note that  $R_{\max} \rightarrow 1$  when  $r_{\text{cyl}} \rightarrow \infty$ ; which is equivalent to  $c \rightarrow 0$  in Fig. 20). The relationship between  $L$ ,  $c$ , and  $R_{\max}$  is illustrated in Fig. 20.

### 5.1. Compression ratio

Although Eqs. 19 through 23 are non-linearly coupled, Eqs. 22 and 23 can provide insight into the piston motion. The first task is to identify the characteristic time. The cycle time is an obvious candidate, but it is not known a priori. Moreover, with the exception of a perfect gas with no losses, the piston paths appearing in Fig. 10 are clearly not symmetric about the dead point ( $\dot{x} = 0$ ). On the other hand, the compression paths are virtually identical. Consequently the piston motion is characterized by the “half-cycle” rather than the “full-cycle” time. To define the half-cycle time ( $\tau_H$ ) let

$$\left. \frac{dV^*}{dt^*} \right|_{t^*=0} = -\frac{\dot{x}_0\tau_H}{LR_{\max}} = -1, \quad (25)$$

where  $\dot{x}_0 = \dot{x}(0)$ , that is, the initial velocity of the piston. Consequently the half-cycle time is given by

$$\tau_H = \frac{LR_{\max}}{\dot{x}_0}, \quad (26)$$

and physically, it approximates the time required to decelerate the piston from  $\dot{x}_0$  to zero (Fig. 20).

Next, the half-cycle time is substituted into Eq. 23. The result is

$$\frac{d^2V^*}{dt^{*2}} = \frac{LR_{\max}P_\infty}{\dot{x}_0^2 (m_p/A_p)} (P^* - 1), \quad (27)$$

which allows us to define a dimensionless “dynamic” parameter,

$$\Gamma = \frac{LR_{\max}A_pP_\infty}{m_p\dot{x}_0^2}. \quad (28)$$

One should note that by definition,  $V^* = 1/r$  (Eq. 17). Therefore, a relationship between the compression ratio and the dynamic parameter,  $\Gamma$  is expected. This hypothesis is confirmed in Fig. 21 where the maximum compression ratios from the parametric cases are plotted versus dynamic parameter. Additionally, the quality of the correlation suggests that equivalence ratio and mass loss are minor influences on the compression ratio. This fact is remarkable because mass loss is known to affect the compression ratio (Section 3.3.2.). Hence, the compression ratio is essentially a function of the dynamic parameter and this has the immediate implication that  $0.045 \leq \Gamma \leq 0.1$

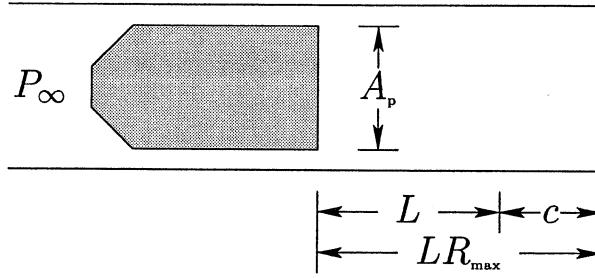


Fig. 20. The relation between the piston initial position, clearance distance  $c$ ,  $R_{\max}$ , and  $L$ . One should note that physically, the piston travel cannot exceed  $L$ .

is optimal because  $50 \leq r \leq 100$  maximizes efficiency (Fig. 18).

Physical insight into the dynamic parameter is gained by recognizing that the product  $LA_p R_{\max}$  is the initial volume of the charge (Fig. 20). Therefore,  $LB_{\max} A_p P_{\infty}$  is the work required to displace this volume to the ambient. Meanwhile,  $m_p x_0^2$  is twice the initial kinetic energy of the piston. This quantity, however, is equal to double the magnitude of the compression work because the final piston velocity is zero. Consequently the dynamic parameter has the physical interpretation

$$\Gamma = \frac{\text{Work required to displace the cylinder contents}}{2 \times \text{Work of compression}} \quad (29)$$

Using this physical interpretation, a dynamic parameter for the isentropic compression of a perfect gas by a free-piston may be developed, that is,

$$\Gamma_p = \frac{P_0 V_0}{(1 - \gamma) m_p x_0^2} \quad (30)$$

In this case, the compression ratio is an explicit function of the dynamic parameter. This function is given by

$$r = \left[ \frac{1}{2\Gamma_p} + 1 \right]^{\frac{1}{\gamma-1}}, \quad (31)$$

and it is plotted in Fig. 22 for specific heat ratios of 1.25, 1.3, 1.35, and 1.4. These plots suggest that variations in the specific heat ratio account for some of the “scatter” in Fig. 21. That is, for a given dynamic parameter, smaller specific heat ratios yield larger compression ratios. Inspection of Fig. 21 reveals that this is indeed the case because for a given dynamic parameter, the largest compression ratios correspond to  $\Phi = 2.9$  (smallest  $\gamma$ ). Therefore, decreasing the specific heat ratio of a mixture “softens” the gas spring. Finally, a comparison of Figs. 21 and 22 reveals that the perfect gas model greatly exag-

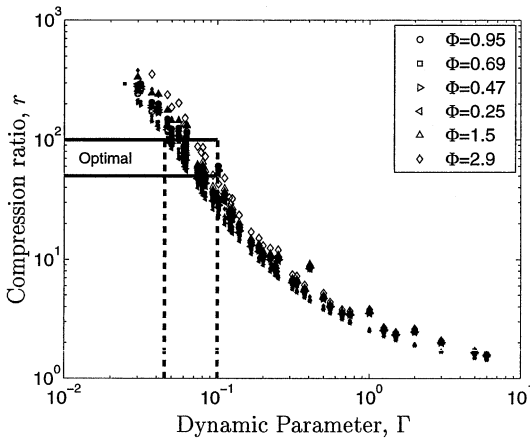


Fig. 21. Compression ratio versus dynamic parameter,  $\Gamma$  for all parametric cases. Open symbols indicate heptane-air and dark symbols denote propane-air cases. Also, smaller symbols represent cases where leakage is neglected.

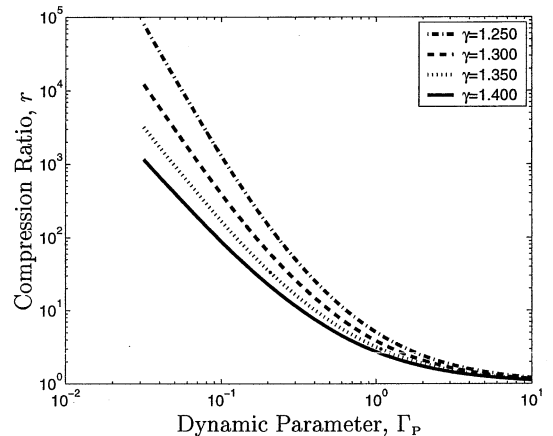


Fig. 22. Compression ratio versus perfect gas dynamic parameter,  $\Gamma_p$  (Eq. 31).

gerates the compression ratio when the dynamic parameter is small, that is,  $\Gamma < 0.1$ . Hence, variable specific heats and other non-linear effects become increasingly significant when the dynamic parameter decreases.

5.2. Percent mass lost

Mass loss is a problem intrinsic to the single-shot process. Presumably, any micro-engine design that features an unsealed piston will have the same problem. Therefore, understanding the relationship between percent mass lost and the initial conditions is essential.

First, the percent mass lost is defined by

$$M_L = \frac{m_0 - m_f}{m_0} \times 100\%, \tag{32}$$

where the initial mass,  $m_0$  is given by  $m_0 = V_0/v_0$ . The percent mass lost is related to the blow-by mass flow rate by integrating Eq. B.1 and substituting the result into Eq. 32; this gives

$$M_L = 100\% \int_0^{\tau_c} \frac{\tau_c v_0 \dot{m}}{V_0} dt. \tag{33}$$

One should note that the “full cycle” time,  $\tau_c$  is used here because mass is lost throughout the process. Next, the integral is non-dimensionalized to yield

$$M_L = 100\% \int_0^{t_c^*} \frac{\tau_H v_0 \dot{m}}{V_0} dt^*, \tag{34}$$

where  $t_c^* = \tau_c/\tau_H$ , is the non-dimensional cycle time. Next, Eq. 4 is substituted for  $\dot{m}$  in Eq. 34; the integrand becomes

$$\frac{\tau_H v_0 \dot{m}}{V_0} = \left(\frac{A_t}{A_c}\right) \frac{\tau_H v_0 P_\infty C_d M(P_\infty P^*, P_\infty, \gamma)}{LR_{\max} (R_m T_0)^{\frac{1}{2}}} \left(\frac{P^*}{T^{*\frac{1}{2}}}\right). \tag{35}$$

Dividing Eq. B.2 by Eq. B.20 and simplifying yields

$$\frac{A_t}{A_c} = \left(\frac{t_G}{D_p}\right) \frac{4(t_G/D_p) + 4}{4(t_G/D_p)^2 + 4(t_G/D_p) + 1}, \tag{36}$$

which can be approximated by

$$\frac{A_t}{A_c} \approx 4\left(\frac{t_G}{D_p}\right), \tag{37}$$

when the gap-to-piston-diameter ratio,  $t_G/D_p$  is small. Consequently the percent mass lost is given by

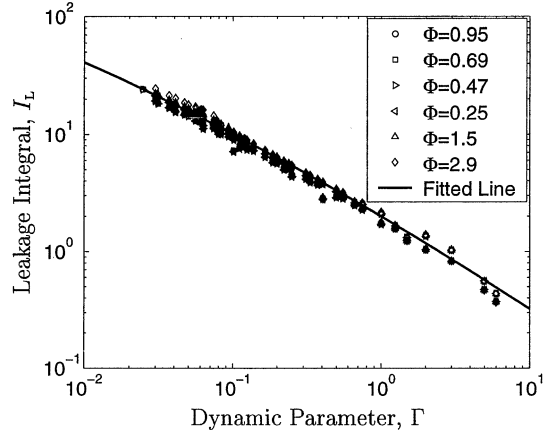


Fig. 23. Leakage integral versus dynamic parameter,  $\Gamma$  for all parametric cases. Open symbols indicate heptane-air and dark symbols denote propane-air cases. Note that  $\gamma = 1.3$  is assumed to compute  $M(P^*, \gamma)$ . The equation of the fitted line is  $I_L = \exp [-0.0195 (\log \Gamma)^2 - 0.7461 \log \Gamma + 0.6920]$ .

$$M_L \approx 100\% \times 4 \left(\frac{t_G}{D_p}\right) \left[ \frac{\tau_H v_0 P_\infty C_d}{LR_{\max} (R_m T_0)^{\frac{1}{2}}} \right] I_L, \tag{38}$$

where  $I_L$  is the “leakage integral.” This integral is defined by

$$I_L = \int_0^{t_c^*} \frac{M(P_\infty P^*, P_\infty, \gamma) P^*}{T^{*\frac{1}{2}}} dt^*, \tag{39}$$

and it depends upon the non-dimensional temperature-pressure history of the charge.

According to Eq. 38, the percent mass lost is inversely proportional to the chamber length. This result is encouraging because it is consistent with Fig. 16. But when the half-cycle time is substituted into Eq. 38, the length dependence disappears viz.,

$$M_L \approx 100\% \times 4\left(\frac{t_G}{D_p}\right) \left[ \frac{v_0 P_\infty C_d}{\dot{x}_0 (R_m T_0)^{\frac{1}{2}}} \right] I_L. \tag{40}$$

Consequently, the leakage integral must account for the chamber length dependence. To investigate this hypothesis, the leakage integral is computed and plotted in Fig. 23 for the various parametric cases.

Clearly, the leakage integral,  $I_L$  is a function of the dynamic parameter,  $\Gamma$ . This integral, however, cannot be expressed in closed form; thus, it is approximated by a second-order curve fit, that is,

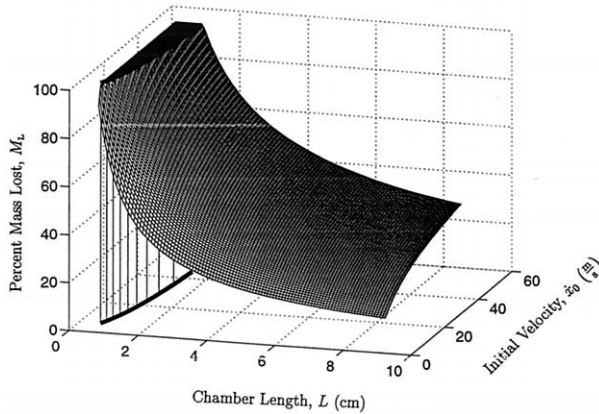


Fig. 24. Predicted percent mass lost versus chamber length and initial velocity. The surface is obtained by substituting Eq. 41 into Eq. 40 and assuming that the fresh charge is air. The curve projected onto the  $x_0$ - $L$  plane denotes 100% mass lost.

$$I_L = \exp[-0.0195 (\log \Gamma)^2 - 0.7461 \log \Gamma + 0.6920]. \quad (41)$$

Next, Eq. 41 is substituted into Eq. 40 to obtain an analytical expression for the percent mass lost in terms of initial conditions. This expression is plotted in Fig. 24 versus  $L$  and  $x_0$ . Evidently, it captures three dependencies: (1) the percent mass lost is most sensitive to the chamber length, (2) the percent mass lost is inversely proportional to the chamber length, and (3) the percent mass lost depends weakly upon the initial velocity. Although relative to Fig. 16, Eqs. 40 and 41 exaggerate the percent mass lost. Additionally, certain combinations of initial velocity and chamber length are incompatible. These combinations are identified in Fig. 24 by projecting the 100% mass lost curve onto the chamber length-initial velocity plane.

To facilitate future design work, a scaling relation for  $M_L$  is developed. First, a simpler approximation for the leakage integral is obtained, that is,

$$I_L = \exp[-0.7015 \log \Gamma + 0.6743]. \quad (42)$$

Next, Eq. 42 is substituted into Eq. 40 and the result is simplified. This gives

$$M_L \approx 100\% \times 9.300 \frac{t_G C_d v_0 P_\infty^{0.2985} x_0^{0.403}}{D_p^{2.403} (R_m T_\infty)^{\frac{1}{2}}} \left( \frac{m_p}{LR_{\max}} \right)^{0.7015}, \quad (43)$$

which sheds considerable light on the mass loss problem. First, Eq. 38 implies that the percent mass lost is proportional to the gap-to-piston-diameter ratio,  $t_G/D_p$ . Equation 43, however, indicates that the piston

diameter dependence is actually much stronger. Therefore, increasing or decreasing the piston diameter will have a considerable effect on the percent mass lost. Second, Eq. 43 predicts that the percent mass lost will *increase*—albeit slowly—with the piston initial velocity; this result is corroborated by Fig. 16. Third, like Eq. 38, Eq. 43 suggests that the percent mass lost is inversely proportional to the chamber length, but this dependence is somewhat weaker. Finally, Eq. 43 reveals that the percent mass lost is proportional to the piston mass. Consequently to reduce the percent mass lost, one may: (1) increase the cylinder length, (2) increase the piston diameter, (3) decrease the gap width, or (4) decrease the piston mass.

## 6. Conclusion

This paper presents results from single-shot micro-HCCI experiments and a detailed chemical kinetic model. The relationship between the initial conditions, leakage, and the indicated fuel conversion efficiency are explored with the aid of a parametric model study. Also, the governing equations are non-dimensionalized to reveal: (1) an appropriate characteristic time, (2) a non-dimensional parameter that essentially determines the compression ratio, and (3) an approximate functional relationship between the initial conditions and the percent mass lost.

The salient findings of this paper are:

1. HCCI is possible in spaces 3 mm diameter and 0.3 mm long.
2. HCCI combustion of heptane at equivalence ratios of  $\Phi = 0.69$  and  $\Phi = 0.25$  is demonstrated.

3. A model which couples free-piston motion and detailed chemical kinetics is developed and used to model the single-shot micro-HCCI experiments.
4. The single-shot numerical model employing detailed chemical kinetics is shown to reproduce piston position and velocity measurements very well.
5. Leakage (blow-by) accounts for:
  - a. A distortion of the piston-time path during the expansion stroke.
  - b. An *increase* in the compression ratio relative to an ideal case.
  - c. A decrease in the fuel conversion efficiency.
6. Percent mass lost may be reduced by:
  - a. Increasing the chamber length.
  - b. Increasing the piston diameter.
  - c. Decreasing the piston-cylinder gap.
  - d. Decreasing the piston mass.
7. The dynamic parameter  $\Gamma$ , is defined by Eq. 28 and it:
  - a. Characterizes the compression process i.e., it captures the relationship between initial conditions and the compression ratio.
  - b. May be interpreted to be the ratio of “The work required to displace the volume swept by the piston to double the compression work.”
  - c. If one assumes that a compression ratio between 50 and 100 is optimal, then the piston mass, initial velocity, and cylinder length must satisfy the constraint  $0.045 \leq \Gamma \leq 0.1$ .

### Acknowledgments

This project was sponsored by Honeywell International under DARPA contract No. F30602-99-C-0200 and the Minnesota Supercomputing Institute. Also, the authors wish to thank Dr. Wei Yang and Mr. Tom Rezachek of Honeywell International.

### A Appendix: Single-shot experiment uncertainty analysis

In the single-shot experiments, movies acquired with the Vision Research Phantom v4.0 digital camera serve three purposes: (1) they indicate that combustion occurs and provide qualitative information, (2) they provide position-time data, and (3) they provide velocity-time data.

The measurements rely upon length and time calibrations. A distance calibration is required for each experiment. Basically, one uses the manufacturer’s

software to relate a known distance to a certain number of pixels. The software then determines the resolution ( $\delta x$ ) and computes distances by counting pixels between user-specified locations. Therefore the physical distance,  $\Delta x$  is determined by

$$\Delta x = (\#Pixels) \delta x. \quad (A.1)$$

Velocity is determined in a similar manner, except that frames are incremented rather than pixels. This is also accomplished through software; the user: (1) marks the initial position of an object, (2) advances the movie one or more frames, and (3) marks the final position of the object. One should note that the same physical location must be marked each time for this method to be accurate. Hence the time increment ( $\Delta t$ ) is computed by

$$\Delta t = (\#Frames) \delta t, \quad (A.2)$$

where  $\delta t$  is the time resolution. Physically, the time resolution is the greater of the shutter speed and the frame refresh rate. In all single-shot experiments, the refresh rate is  $16 \mu s$  and it is the larger quantity. For the purposes of this analysis, this quantity is assumed exact.

The velocity ( $\tilde{V}$ ) is computed with

$$\tilde{V} = \frac{\Delta x}{\Delta t}. \quad (A.3)$$

The velocity relative uncertainty is, therefore, given by

$$\left(\frac{U_{\tilde{V}}}{\tilde{V}}\right)^2 = \left(\frac{\delta x}{\Delta x}\right)^2 + \left(\frac{\delta t}{\Delta t}\right)^2, \quad (A.4)$$

when resolutions and uncertainties are assumed to be identical. If Eqs. A.1 and A.2 are substituted into Eq. A.4, however, the result is

$$\left(\frac{U_{\tilde{V}}}{\tilde{V}}\right)^2 = \left(\frac{1}{\#Pixels}\right)^2 + \left(\frac{1}{\#Frames}\right)^2. \quad (A.5)$$

Hence the velocity relative uncertainty depends upon the number of pixels traveled and the number of frames elapsed. The camera field of view is 32 pixels high and 256 pixels long. In contrast, the entire compression process, that is, from initial velocity to zero, occurs in tens of frames. Consequently, the number of pixels traveled is always much greater than the number of frames elapsed. Therefore, the velocity relative uncertainty is

$$\frac{U_{\tilde{V}}}{\tilde{V}} \sim \frac{1}{\#Frames}. \quad (A.6)$$

Velocity measurements are usually taken over two or five frames because the piston velocity changes quickly. Thus, velocity relative uncertainties are un-

Table A.1

Typical measurements from a single-shot experiment. These measurements are obtained with a micrometer and dial calipers

Quantity	Value
$L$	34.87 mm
$U_L$	0.03 mm
$d$	0.3 mm
$U_d$	0.1 mm

avoidably between 20 and 50%; hence piston velocity measurements are considered approximate.

Experiments have yielded the observation that ignition depends chiefly upon the geometric compression ratio. The geometric compression ratio is computed with

$$r = \frac{L}{d}, \tag{A.7}$$

where  $L$  is the initial distance between the piston and end plug (see Fig. 2) and  $d$  is the minimum distance. The compression ratio relative uncertainty is therefore, given by

$$\left(\frac{U_r}{r}\right)^2 = \left(\frac{U_L}{L}\right)^2 + \left(\frac{U_d}{d}\right)^2. \tag{A.8}$$

Typical experimental values are given in Table A.1. When these values are substituted into Eqs. A.7 and A.8, one obtains  $r = 120 \pm 40$ . Hence measurements of the geometric compression ratio are also approximate at best. This result is also unavoidable because the right hand term dominates Eq. A.8.

That is,

$$\frac{U_r}{r} \sim \frac{\delta x}{d}, \tag{A.9}$$

hence this measurement is limited by the camera resolution.

### B Appendix: Derivation of the model equations

The detailed derivation of the single-shot model equations is presented in this section. One should refer to Fig. 6 for the definitions of the geometric parameters and Section 3.1. for the model assumptions.

#### B.1. Mass balance

A mass balance applied to the control volume gives

$$\frac{dm_{cv}}{dt} + \dot{m} = 0. \tag{B.1}$$

where  $\dot{m}$  is the mass flow rate of escaping gas. Alternatively, Eq. B.1 may be expressed in terms of the cylinder volume,  $V$  and specific volume,  $v$  by making the substitution  $m_{cv} = V/v$ . The result is

$$\frac{1}{v} \frac{dV}{dt} - \frac{V}{v^2} \frac{dv}{dt} + \dot{m} = 0. \tag{2}$$

Also, the blow-by mass flow rate is assumed to be given by

$$\dot{m} = \frac{C_d A_t P}{(R_m T)^{\frac{1}{2}}} M(P, P_\infty, \gamma), \tag{4}$$

where

$$M(P, P_\infty, \gamma) =$$

$$\left\{ \left(\frac{P_\infty}{P}\right)^{\frac{1}{\gamma}} \left\{ \frac{2\gamma}{\gamma-1} \left[ 1 - \left(\frac{P_\infty}{P}\right)^{\frac{\gamma-1}{\gamma}} \right] \right\}^{\frac{1}{2}} \right. \\ \left. \gamma^{\frac{1}{2}} \left(\frac{2}{\gamma+1}\right)^{\frac{1}{2(\gamma-1)}} \right\}$$

$$\frac{P_\infty}{P} > \left(\frac{2}{\gamma+1}\right)^{\frac{\gamma}{\gamma-1}} \\ \frac{P_\infty}{P} \leq \left(\frac{2}{\gamma+1}\right)^{\frac{\gamma}{\gamma-1}}, \tag{5}$$

and  $A_t$  is the area of the piston-cylinder gap. This area is defined by

$$A_t = \frac{\pi}{4} (B^2 - D_p^2). \tag{B.2}$$

A mass balance on species  $k$  yields

$$\frac{dm_k}{dt} = \dot{m}_k''' V - \dot{m}_k, \tag{B.3}$$

where  $\dot{m}_k'''$  is the volumetric rate of creation of species  $k$ . Next, if one assumes that  $\dot{m}_k = \dot{m} Y_k$  and substitutes  $m_k = Y_k m_{cv}$  and  $\dot{m}_k''' = \dot{\omega}_k W_k$  into Eq. B.3, then

$$m_{cv} \frac{dY_k}{dt} = \dot{\omega}_k M_k V - Y_k \left[ \dot{m} + \frac{dm_{cv}}{dt} \right] \tag{B.4}$$

results. The quantity in square brackets however, is Eq. B.1. Therefore, Eq. B.4 reduces to

$$\frac{dY_k}{dt} = v \dot{\omega}_k W_k, \tag{6}$$

which interestingly, is exactly the same expression that one would obtain if mass loss had been neglected.

## B.2. Energy balance

Applying an energy balance to the control volume yields

$$\frac{dU_{cv}}{dt} = \dot{Q} - \dot{W} - \dot{m}h. \quad (\text{B.5})$$

Next,  $U_{cv} = m_{cv}u$  and

$$u = \sum_{k=1}^{N_s} u_k Y_k, \quad (\text{B.6})$$

are differentiated to yield

$$\frac{dU_{cv}}{dt} = m_{cv} \frac{du}{dt} + u \frac{dm_{cv}}{dt}, \quad (\text{B.7})$$

and

$$\frac{du}{dt} = \sum_{k=1}^{N_s} u_k \frac{dY_k}{dt} + \sum_{k=1}^{N_s} Y_k \frac{du_k}{dt}, \quad (\text{B.8})$$

respectively. Then

$$u_k = c_{vk}T, \quad (\text{B.9})$$

is differentiated and substituted into Eq. B.8 along with

$$c_v = \sum_{k=1}^{N_s} c_{vk} Y_k, \quad (\text{B.10})$$

and Eq. 6. The result is

$$\frac{du}{dt} = v \sum_{k=1}^{N_s} u_k \dot{\omega}_k W_k + c_v \frac{dT}{dt}. \quad (\text{B.11})$$

Equations B.5 and B.7 are next used to eliminate  $dU_{cv}/dt$ . This gives

$$m_{cv} \frac{du}{dt} = \dot{Q} - \dot{W} - \dot{m}h - u \frac{dm_{cv}}{dt}, \quad (\text{B.12})$$

but when Eq. B.1 is substituted for  $\dot{m}$ , one obtains

$$m_{cv} \frac{du}{dt} = \dot{Q} - \dot{W} + (h - u) \frac{dm_{cv}}{dt}, \quad (\text{B.13})$$

which in turn, reduces to

$$m_{cv} \frac{du}{dt} = \dot{Q} - \dot{W} + P v \frac{dm_{cv}}{dt}. \quad (\text{B.14})$$

Next, the work and heat transfer terms are assumed to be

$$\dot{W} = P \frac{dV}{dt}, \quad (\text{B.15})$$

and

$$\dot{Q} = m_{cv} \dot{q}, \quad (\text{B.16})$$

respectively. The rate of heat loss per unit mass,  $\dot{q}$  and the average heat flux,  $\bar{q}''$  are given by

$$\dot{q} = \frac{v}{V} \left[ \frac{\pi B^2}{2} + \pi B(L - x) \right] \bar{q}'', \quad (9)$$

and

$$\bar{q}'' = \frac{2k_T(T - T_w)}{(L - x)} \cdot \left[ \frac{0.440332\pi^2 + 5.09296 \left( \frac{L - x}{B} \right)^2}{\pi + 2\pi \left( \frac{L - x}{B} \right)} \right]. \quad (10)$$

The derivation of Eqs. 9 and 10 is discussed in Section 3.1.

Substituting Eqs. B.15 and B.16 into Eq. B.14 gives

$$m_{cv} \frac{du}{dt} = m_{cv} \dot{q} - P \frac{dV}{dt} + P v \left[ \frac{1}{v} \frac{dV}{dt} - \frac{V}{v^2} \frac{dv}{dt} \right], \quad (\text{B.17})$$

and this reduces to

$$\frac{du}{dt} = \dot{q} - P \frac{dv}{dt}, \quad (\text{B.18})$$

after canceling terms. Lastly, Eq. B.11 is substituted into Eq. B.18 and rearranged to yield

$$c_v \frac{dT}{dt} + v \sum_{k=1}^{N_s} u_k \dot{\omega}_k W_k - \dot{q} + P \frac{dv}{dt} = 0. \quad (7)$$

Like Eq. 6, Eq. 7 is exactly the same expression that one would obtain if blow-by were neglected. Consequently, Eq. 2 which relates density to cylinder volume, is the only expression in which mass loss appears.

## B.3. Force balance

Next, a force balance is applied to the piston, but only gas pressure forces are considered, that is, the piston is frictionless. To ascertain the validity of this assumption, a single-shot experiment was conducted with the end plug removed. The position data is plotted in Fig. B.1 and it reveals that the velocity is constant; which validates our assumption.

To proceed with the force balance, the volume of the combustion chamber is first defined

$$V(x) = A_c(L - x) + V_c, \quad (\text{B.19})$$

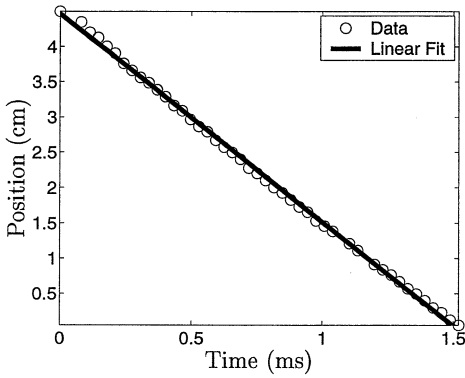


Fig. B.1.

Position data from a single-shot experiment with the end plug removed. The slope of the fitted line is  $-29.5 \frac{\text{m}}{\text{s}}$ .

where  $V_c$  is the clearance volume and  $A_c$  is the cylinder cross-sectional area. This area is defined by

$$A_c = \frac{\pi B^2}{4}. \tag{B.20}$$

Similarly, the piston cross-sectional area is defined

$$A_p = \frac{\pi D_p^2}{4}. \tag{B.21}$$

Next, Eq. (B.19) is differentiated twice to yield

$$\frac{dV}{dt} = -A_c \frac{dx}{dt} \tag{B.22}$$

and

$$\frac{d^2V}{dt^2} = -A_c \frac{d^2x}{dt^2}. \tag{B.23}$$

Consequently applying a force balance on the piston yields

$$m_p \frac{d^2x}{dt^2} = A_p(P_\infty - P), \tag{B.24}$$

which may be expressed in terms of the cylinder volume by substituting Eq. B.24 into Eq. B.23; this gives

$$\frac{d^2V}{dt^2} = -\frac{A_c A_p (P_\infty - P)}{m_p}. \tag{11}$$

#### B.4. Geometric relations

This model employs several geometric parameters and the relations between them. For instance,  $A_t$

$= A_c - A_p$ . Additionally, the piston-cylinder gap is defined by

$$t_G = \frac{B - D_p}{2}. \tag{3}$$

Consequently the gap area,  $A_t$  is also given by

$$A_t = \frac{\pi t_G}{2} (B + D_p). \tag{B.25}$$

Additionally, dividing Eq. B.2 by Eq. B.20 and simplifying yields

$$\frac{A_t}{A_c} = \left( \frac{t_G}{D_p} \right) \frac{4(t_G/D_p) + 4}{4(t_G/D_p)^2 + 4(t_G/D_p) + 1}, \tag{36}$$

and one can show that it becomes

$$\frac{A_t}{A_c} \approx 4 \left( \frac{t_G}{D_p} \right), \tag{37}$$

when  $t_G/D_p \rightarrow 0$ .

#### References

- [1] W. Yang, U. Bonne, et al. MEMS free-piston knock engine. Technical Proposal, DARPA Contract F30602-99-C-0200, 1999. Honeywell Technology Center, 12001 State Highway 55, Plymouth, MN 55441.
- [2] A.H. Epstein, S.D. Senturia, G. Anathasuresh, et al. In: Transducers '97 Chicago: Digest of Technical Papers. IEEE, Chicago, 1997 pp. 753–756.
- [3] C. Fernandez-Pello, D. Liepmann, A. Pisano, et al. MEMS rotary combustion laboratories. University of California at Berkeley Internet Document (Last loaded July 2001), 2001. URL <http://www.me.berkeley.edu/mrcl/>.
- [4] W. Yang, U. Bonne, B.R. Johnson. Microcombustion engine/generator. U. S. Patent 6,276,313, 2001.
- [5] M. Allen, et al. Research topics-miniature MEMS free-piston engine generator. Georgia Institute of Technology Internet Document (Last loaded July 2001), 2001. URL <http://comblab5.ae.gatech.edu/Minipiston/intro.htm>.
- [6] H.T. Aichlmayr, D.B. Kittelson, M.R. Zachariah, Chem Eng Sci 57(19) (2002) 4161–4171.
- [7] I.A. Waitz, G. Gauba, Y. Tzeng, Fluids Engine 120 (1) (1998) 109–117.
- [8] S. Onishi, S.H. Jo, K. Shoda, P.D. Jo, S. Kato. SAE Technical Paper 790501 (1979).
- [9] N. Iida. SAE Technical Paper 940684 (1994).
- [10] J. Lavy, P. Duret, P. Habert, E. In: Selected Presentations from the Second International Workshop and Thematic Network Meeting on Modernised 2/Stroke Engines, The 2/Stroke Thematic Network Circular. Manchester, UK, 1996 pp. 1–9.
- [11] R. Gentili, S. Frigo, L. Tognotti, et al. SAE Technical Paper 970363 (1997).

- [12] P.M. Najt, D.E. Foster. SAE Technical Paper 830264 (1983).
- [13] R.H. Thring. SAE Technical Paper 892068 (1989).
- [14] H.T. Aichlmayr, D.B. Kittelson, M.R. Zachariah, *Chem Eng Sci* 57(19) (2002) 4173–4186.
- [15] P. Van Blarigan, N. Paradiso, S.S. Goldsborough. SAE Technical Paper 982484 (1998).
- [16] S.S. Goldsborough, P. Van Blarigan. SAE Technical Paper 990619 (1999).
- [17] P. Van Blarigan. Free-piston engine. U. S. Patent 6,199,519, 2001.
- [18] H.T. Aichlmayr. Design Considerations, Modeling and Analysis of Micro-Homogeneous Charge Compression Ignition Combustion Free-Piston Engines. Ph.D. thesis, The University of Minnesota, 2002.
- [19] H.T. Aichlmayr. A review of free-piston engine history, fundamentals and applications. 2003. Manuscript in preparation; to be submitted to *ASME J. for Gas Turbines and Power*.
- [20] A.E. Lutz, R.J. Kee, J.A. Miller. SENKIN: A Fortran Program for Predicting Homogeneous Gas Phase Chemical Kinetics with Sensitivity Analysis. Sandia Rep. SAND87-8248, Sandia National Laboratories, 1988.
- [21] R.J. Kee, F.M. Rupley, E. Meeks. CHEMKIN-III: A Fortran Chemical Kinetics Package for the Analysis of Gas-Phase Chemical and Plasma Kinetics. Sandia Rep. SAND96-8216, Sandia National Laboratories, 1996.
- [22] H.J. Curran, P. Gaffuri, W.J. Pitz, C.K. Westbrook, *Comb Flame* 114 (1998) 149–177.
- [23] N.M. Marinov, W.J. Pitz, C.K. Westbrook, A.M. Vincitore, M.J. Castaldi, S.M. Senkan, C.F. Melius. *Comb Flame* 114 (1998) 192–213.